

Central Washington University
ScholarWorks@CWU

All Faculty Scholarship for the College of the
Sciences

College of the Sciences

2013

Comparison of Earthquake Source Models for the 2011 Tohoku Event Using Tsunami Simulations and Near-Field Observations

Breanyn MacInnes

Hokkaido University, macinnes@geology.cwu.edu

Aditya Riadi Gusman


Hokkaido University

Randall J. LeVeque

University of Washington - Seattle Campus

Yuichiro Tanioka

Follow this and additional works at: <http://digitalcommons.cwu.edu/cotsfac>

 Part of the [Environmental Indicators and Impact Assessment Commons](#), [Environmental Monitoring Commons](#), and the [Geophysics and Seismology Commons](#)

Recommended Citation

MacInnes, B.T., Gusman, A.R., LeVeque, R.J., & Tanioka, Y. (2013). Comparison of earthquake source models for the 2011 Tohoku event using Tsunami simulations and near field observations. *Bulletin of the Seismological Society of America*, 103(28), 1256-1274. DOI: 10.1785/0120120121

This Article is brought to you for free and open access by the College of the Sciences at ScholarWorks@CWU. It has been accepted for inclusion in All Faculty Scholarship for the College of the Sciences by an authorized administrator of ScholarWorks@CWU.

Bulletin of the Seismological Society of America

This copy is for distribution only by
the authors of the article and their institutions
in accordance with the Open Access Policy of the
Seismological Society of America.

For more information see the publications section
of the SSA website at www.seismosoc.org



THE SEISMOLOGICAL SOCIETY OF AMERICA
400 Evelyn Ave., Suite 201
Albany, CA 94706-1375
(510) 525-5474; FAX (510) 525-7204
www.seismosoc.org

Comparison of Earthquake Source Models for the 2011 Tohoku Event Using Tsunami Simulations and Near-Field Observations

by Breanyn T. MacInnes,* Aditya Riadi Gusman, Randall J. LeVeque, and Yuichiro Tanioka

Abstract Selection of the earthquake source used in tsunami models of the 2011 Tohoku event affects the simulated tsunami waveform across the near field. Different earthquake sources, based on inversions of seismic waveforms, tsunami waveforms, and Global Positioning System (GPS) data, give distinguishable patterns of simulated tsunami heights in many locations in Tohoku and at near-field Deep-ocean Assessment and Reporting of Tsunamis (DART) buoys. We compared 10 sources proposed by different research groups using the GeoClaw code to simulate the resulting tsunami. Several simulations accurately reproduced observations at simulation sites with high grid resolution. Many earthquake sources produced results within 20% difference from the observations between 38° and 39° N, including realistic inundation on the Sendai plain, reflecting a common reliance on large initial seafloor uplift around 38° N ($\pm 0.5^\circ$), 143.25° E ($\pm 0.75^\circ$). As might be expected, DART data was better reproduced by sources created by inversion techniques that incorporated DART data in the inversion. Most of the earthquake sources tested at sites with high grid resolution were unable to reproduce the magnitude of runup north of 39° N, indicating that an additional source of tsunamigenic energy, not present in most source models, is needed to explain these observations.

Online Material: Figures of buoy, inundation and run-up simulations and observations, associated data sets, and simulation code.

Introduction

The catastrophe of the 11 March 2011 Tohoku earthquake and tsunami in Japan has opened unprecedented avenues for understanding the dynamics of both earthquakes and tsunamis. Numerous data and detailed documentation, including instrumental measurements by seismometers, Global Positioning System (GPS) receivers, tide gauges, ocean-bottom pressure sensors, or other instruments, as well as numerous forms of multimedia and eyewitness accounts, will enable studies of the 2011 Tohoku event to continue for years. For tsunami science, the density of observations will inspire future investigations of tsunami erosion, sediment transportation, tsunami propagation, or onshore flow dynamics. However, future research that requires simulation of the tsunami will encounter the daunting task of choosing an earthquake source that most accurately recreates the tsunami's characteristics.

Advances in inversion techniques have led to a proliferation in earthquake source models following major earthquakes; the 2011 Tohoku event is no exception as

published slip distributions for the 2011 Tohoku earthquake number in the dozens (e.g., Ammon *et al.*, 2011; Fujii *et al.*, 2011; Hayes, 2011; Iinuma *et al.*, 2011; Koketsu *et al.*, 2011; Lay *et al.*, 2011; Maeda *et al.*, 2011; Saito *et al.*, 2011; Simons *et al.*, 2011; Gusman *et al.*, 2012; Tang *et al.*, 2012; Wei *et al.*, 2012). Slip distribution inversions provide a means of estimating the complex seafloor-deformation patterns associated with major earthquakes and become the initial conditions for tsunami models. However, the number and diversity of slip distributions for recent tsunamigenic events leave tsunami modelers with too many choices for initial conditions.

Inaccurate selection of a source model is often pointed to as a source of error in tsunami-inundation simulations (e.g., Arcas and Titov, 2009). Our study focuses on determining the effect of earthquake source selection on the accuracy of replicating the 2011 Tohoku tsunami observations near the earthquake source (the near field) both in the open ocean and on land. In this study, we simulate tsunami propagation and inundation from slip distributions for the 2011 Tohoku earthquake obtained by previous studies. These slip distributions are inferred from different types of data such as tsunami

*Now at Department of Geological Sciences, Central Washington University, 400 E. University Way, Ellensburg, Washington 98926.

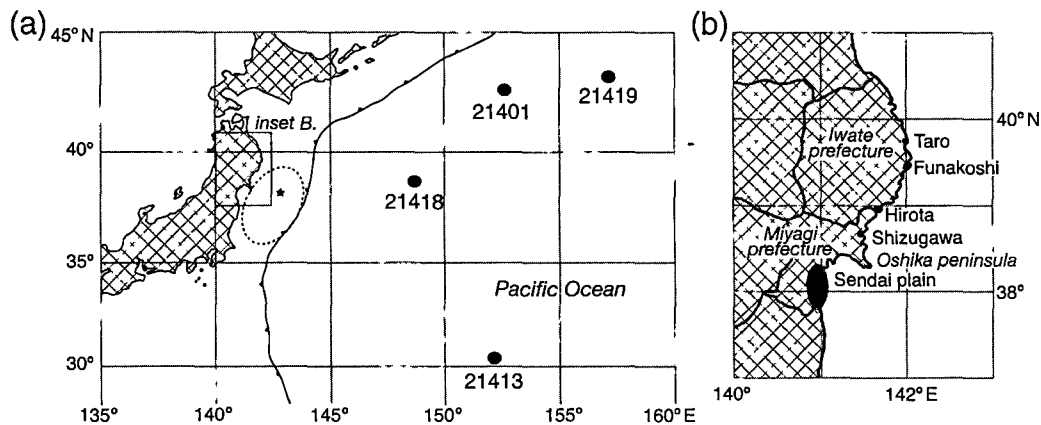


Figure 1. (a) Setting of the 2011 Tohoku earthquake and the DART buoys used in this study. Dashed line represents the approximate area of the 2011 Tohoku earthquake rupture zone; star is the epicenter location. (b) Locations of inundation simulations along the Tohoku coastline and place names referred to in the text. The coastline north of 38.3° N is known as the Sanriku coast. The color version of this figure is available only in the electronic edition.

waveforms, seismic waveforms, and GPS data. We use non-linear shallow-water equations formulated in the tsunami model GeoClaw and compare the observed tsunami waveforms and tsunami heights with simulated results.

Background

The 2011 Tohoku Earthquake and Tsunami

The M_w 9.0 2011 Tohoku earthquake ruptured the plate boundary on 05:46:24 UTC, 11 March 2011, off the Pacific coast of northeastern Honshu, Japan (Figs. 1 and 2). Most slip is predicted to have occurred in the first 60–80 s (Ammon *et al.*, 2011; Ide *et al.*, 2011; Koper *et al.*, 2011). The major slip region is approximately 150-km wide by 300-km long, which is relatively compact compared with the aftershock region (Ammon *et al.*, 2011; Pollitz *et al.*, 2011). The major slip region extends all the way to the Japan trench; large maximum slip has been estimated to be between 30 and 45 m (Fujii *et al.*, 2011; Saito *et al.*, 2011; Gusman *et al.*, 2012; Tang *et al.*, 2012; Wei *et al.*, 2012).

New and recent instrumentation of the Pacific Ocean provided numerous open-ocean measurements of the 2011 Tohoku tsunami waveform, including the extensive global Deep-ocean Assessment and Reporting of Tsunamis (DART) buoy system, operated by the National Oceanic and Atmospheric Administration (NOAA). The four closest DART buoys to Japan, 21418, 21401, 21419, and 21413 (Fig. 1), measured maximum amplitudes of 1.86, 0.77, 0.66, and 0.54 m, respectively (Fig. 3). Besides the DART network, a number of other ocean-bottom pressure sensors and GPS wave buoys measured the tsunami in the deformation area of the 2011 Tohoku event, although these records were not used in this study.

The tsunami was locally devastating, with wave heights of up to 40 m in northern Japan. Post-tsunami fieldwork along the coast of Japan provided more than 5200 measure-

ments of inundation, including tsunami height and runup (Mori *et al.*, 2012). Hereafter, inundation is defined as any location in which the tsunami was on shore, runup is defined as the water height above sea level at maximum inundation, and tsunami height is the elevation of the water surface at any point of inundation other than the maximum. The inland inundation limit of the tsunami was also mapped in every major town in the Sanriku coast and Sendai area. Tsunami heights and runup generally increased from 36° to 39° N, with the exception of lower elevations recorded at the Sendai plain (Fig. 4). Maximum runup and tsunami heights occurred between ~39° and 40° N, with a relatively sharp decrease north of 40° N. In the region of the maximum measured tsunami, the tsunami heights and runups were generally 10–20 m, with an average value of 15 m (Shimozono *et al.*, 2012); of the 1700 data points between 39° and 40° N, approximately 300 points are over 20 m (Mori *et al.*, 2012). These > 20 m points were usually at the heads of V-shaped bays or at the apexes of peninsulas (Shimozono *et al.*, 2012).

Locations for detailed comparisons of simulations and observations in this study include the Sendai plain and four other locations along the Sanriku coast shown in Figure 1. Along the Sendai plain, inundation reached over 5 km inland (generally 3–4 km), albeit with low runup (0–4 m) in much of the area (Fig. 5a). Highest tsunami heights, generally 5–10 m, occurred within 1 km of the shoreline. At the narrower southern end of the Sendai plain, inundation was only 1–2 km and runup was much higher, generally 5–12 m. Cameras at Sendai airport, 1 km from the shoreline, recorded the arrival of the tsunami at 71 min after the earthquake initiated.

In the Shizugawa district of Minamisanriku town, the tsunami heights peaked at 18 m and runup values ranged from 9 to 16 m (Fig. 6a). Heights of 13–15 m occurred in the center of town. Inundation continued as far as 3 km inland, following river valleys into the mountainous terrain. Inundation near Hirota (a town in Rikuzentakata city)

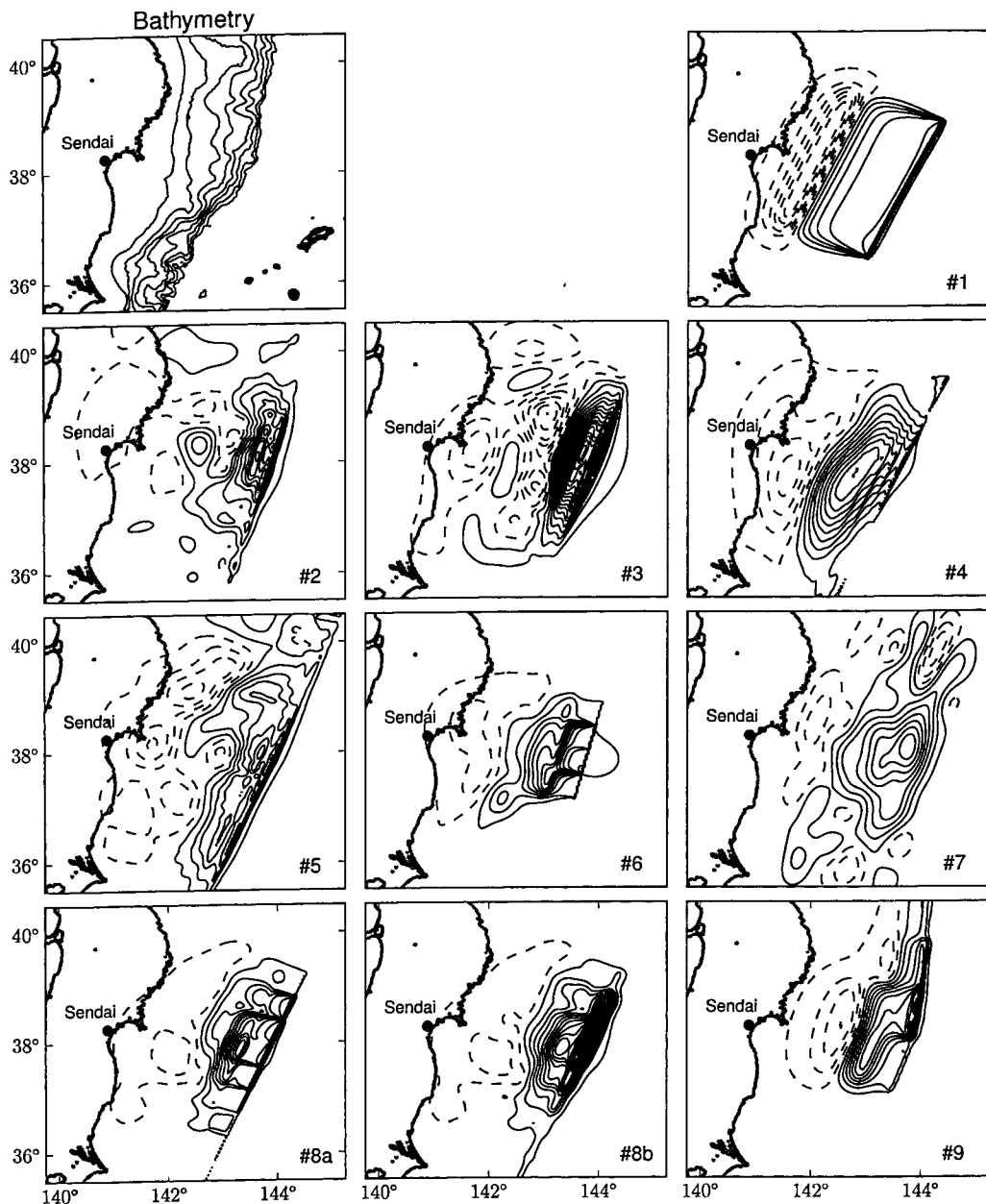


Figure 2. Bathymetry (top left) and sea surface deformation patterns of each inversion simulated in this study; names for each inversion are located in the lower right corners. Contours of bathymetry (top left) are at 500-m increments from -500 to -4000 m. Meters of vertical displacement are indicated at contour levels 0.5 m, 1.5 m, and so on (solid lines) and -0.5 m, -1.5 m, and so forth (dashed lines). Deformation patterns were calculated using the Okada (1985) equations, with the exception of 7, 8b, and 9, which were provided by the authors of previous studies (7: Saito *et al.*, 2011; 8: Gusman *et al.*, 2012; 9: Tang *et al.*, 2012; also 9: Wei *et al.*, 2012). The color version of this figure is available only in the electronic edition.

roughly followed topographic contours on both sides of the 1.5-km-wide isthmus, at maximum 700 m inland, and almost crossing at a saddle. Runup was higher on the Ono Bay side (12–16 m) than the Hirota Bay side (10–11 m; Fig. 7a). In contrast to the Hirota area, the low, 1.5-km-wide isthmus where the Funakoshi district of Yamada town was completely overtopped by the tsunami. Tsunami runup was more variable and generally higher on the south side (12–19 m) than the north side (14–15 m) of the isthmus and tsunami

heights of 10–13 m were measured in the center of the inundated area (Fig. 8a). In the Taro district of Miyako city, two 7.8-m-high (10 m above sea level) tsunami seawalls crossed the town in the east–west and northeast–southwest directions; the eastern wall was partially destroyed during inundation. Tsunami heights behind the remaining seawalls were generally less than 10 m, but were 15–20 m near the port (Fig. 9a). Inundation distance in Taro was 1.5 km at maximum and generally 0.5 km.

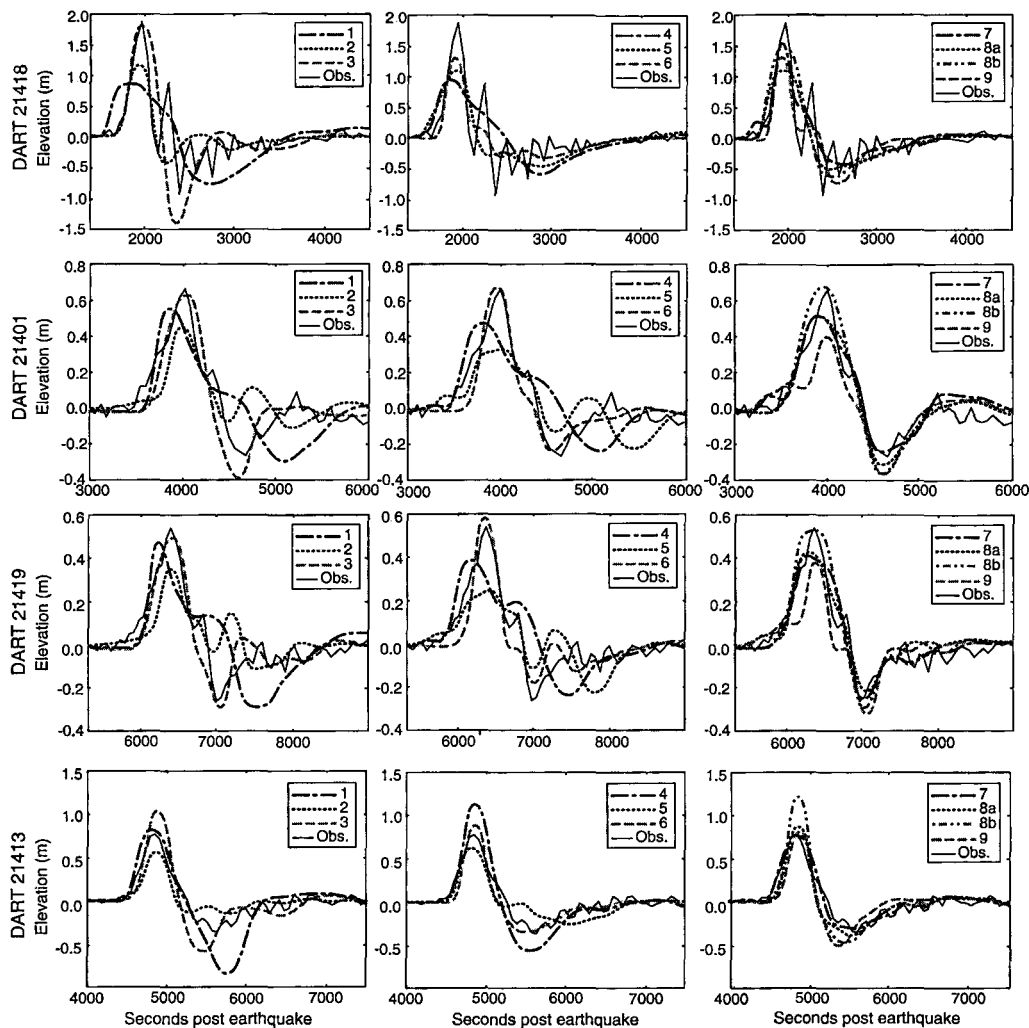


Figure 3. Plots of simulated tsunami waveforms for all source models 1–9 compared to actual observations at the four closest DARTs to Japan. Waveforms have been shifted by the optimal T_d (Table 2). For unshifted waveforms, see © Figure S1 in the electronic supplement. The color version of this figure is available only in the electronic edition.

Earthquake Sources

Inversions for slip distribution during the earthquake use a variety of geophysical records of the event, including seismological, GPS, and tsunami waveform data (Ammon *et al.*, 2011; Fujii *et al.*, 2011; Hayes, 2011; Saito *et al.*, 2011; Shao *et al.*, 2011; S. Wei *et al.*, 2011; Gusman *et al.*, 2012; Tang *et al.*, 2012; Wei *et al.*, 2012). The inversions simulated in this study, designated with labels 1–9 (Table 1), all determine maximum coseismic slip adjacent to the southern Sanriku coast and Sendai plain. Primary differences in inversion solutions are the position or depth of maximum slip relative to the trench and the magnitude of maximum slip.

Earthquake-source models selected for this study were chosen based on their methodological differences. Source models incorporating seismic data used in this study (see Table 1 for citations) inverted teleseismic P , SH , and long-period waves (sources 2 and 3), P and Rayleigh waves with GPS station motion (4), and P , SH , and long-period waves

with GPS station motion (5). Source models derived from tsunami waveforms used DART records only (9) or DART records combined with offshore GPS wave gauges and cabled bottom-pressure gauges (7). Open-ocean tsunami records were also combined with coastal tide-gauge tsunami records (6) or GPS and seafloor crustal deformation data (8a and 8b). Source 8b differs from that of 8a in that 8b assumed additional uplift from the unconsolidated sedimentary wedge near the trench, after Tanioka and Seno (2001). Seismic sources 2–4 include rupture timing and duration in their inversion calculations. Tsunami inversions (6–9) do not include timing, with the exception of 6, which assumes that deformation occurs over 30-s duration (rise time) for all subfaults simultaneously (Table 1). Tsunami models often assume instantaneous rupture, rather than finite rupture duration. Source 1, created for this study, parameterizes uniform slip transcribed onto the fault plane determined by the Global centroid moment tensor (GCMT) solution (see Data and Resources) and represents the simplest input needed

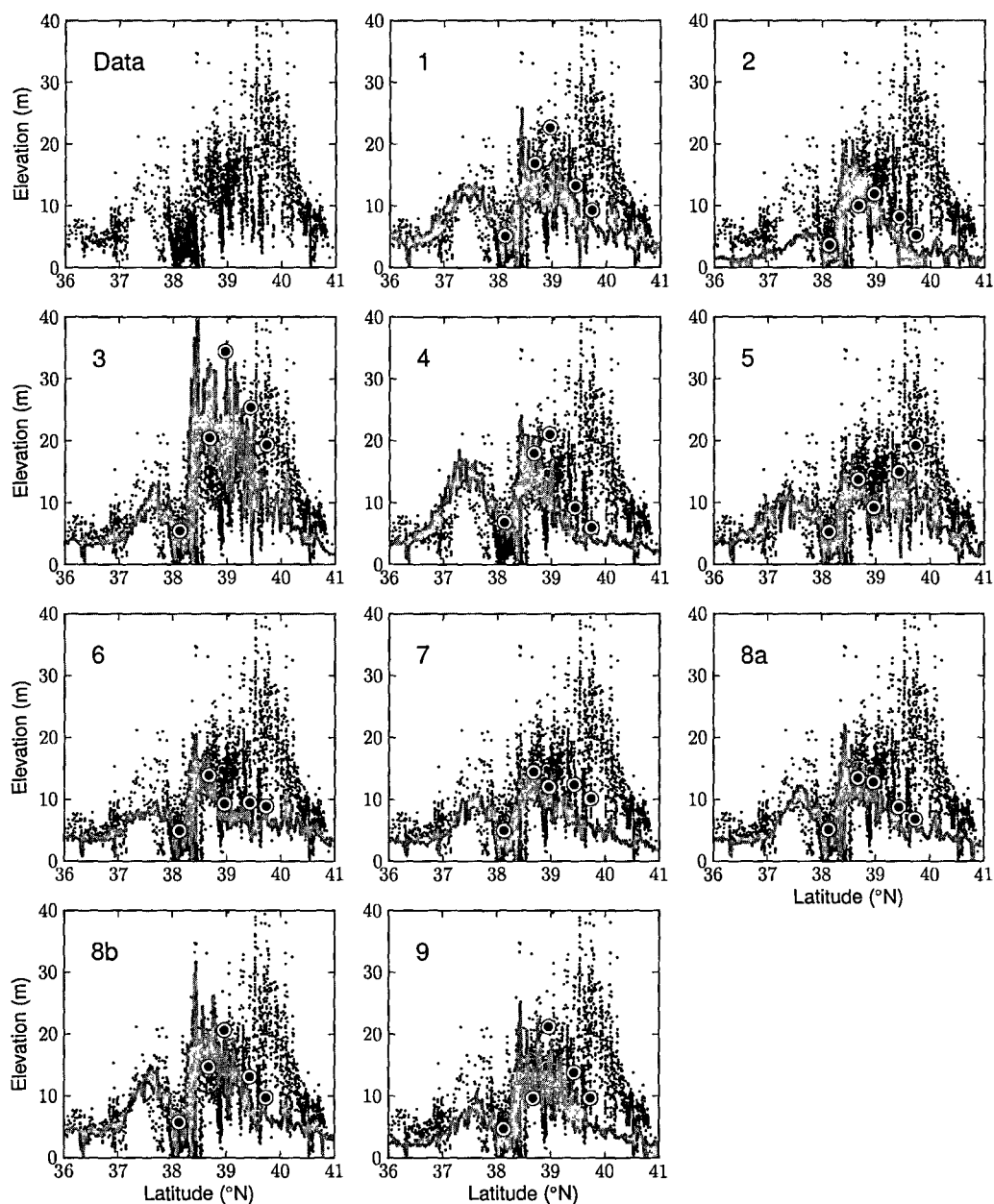


Figure 4. Observations of the 2011 Tohoku tsunami (small black dots) along the Pacific coast of Honshu compared to simulated tsunami runup (line) for all earthquake sources. These simulations were run to $90''$ resolution grids, which is too low a resolution to give reliable results in the complex topography of Sanriku. Larger black dots represent the maximum tsunami simulated by the high-resolution runs in Sendai plain, Shizugawa, Hirota, Funakoshi, and Taro (from left to right). Better results were obtained from higher resolution modeling although not every simulation showed notable improvement; see Figures 5–9 and © Figures S3–S12 in the electronic supplement. The color version of this figure is available only in the electronic edition.

for a tsunami model to simulate the 2011 Tohoku earthquake. Source 1 assumes uniform slip of 29.5 m based on the GCMT seismic moment over a rupture zone comparable to that of sources 4, 8a, and 8b.

Methods

GeoClaw Tsunami Propagation

The GeoClaw model used to perform the simulations presented below is an open-source software package that

has recently been approved by the United States National Tsunami Hazard Mitigation Program (NTHMP) for use in hazard-modeling products, following a benchmarking process described in Gonzalez *et al.* (2011). The software and numerical algorithms are further described in Berger *et al.* (2011), George (2008), and George and LeVeque (2006). These papers include verification and validation on additional test problems. The two-dimensional shallow-water equations are solved using a wave-propagation finite volume method of the type described in more detail in LeVeque

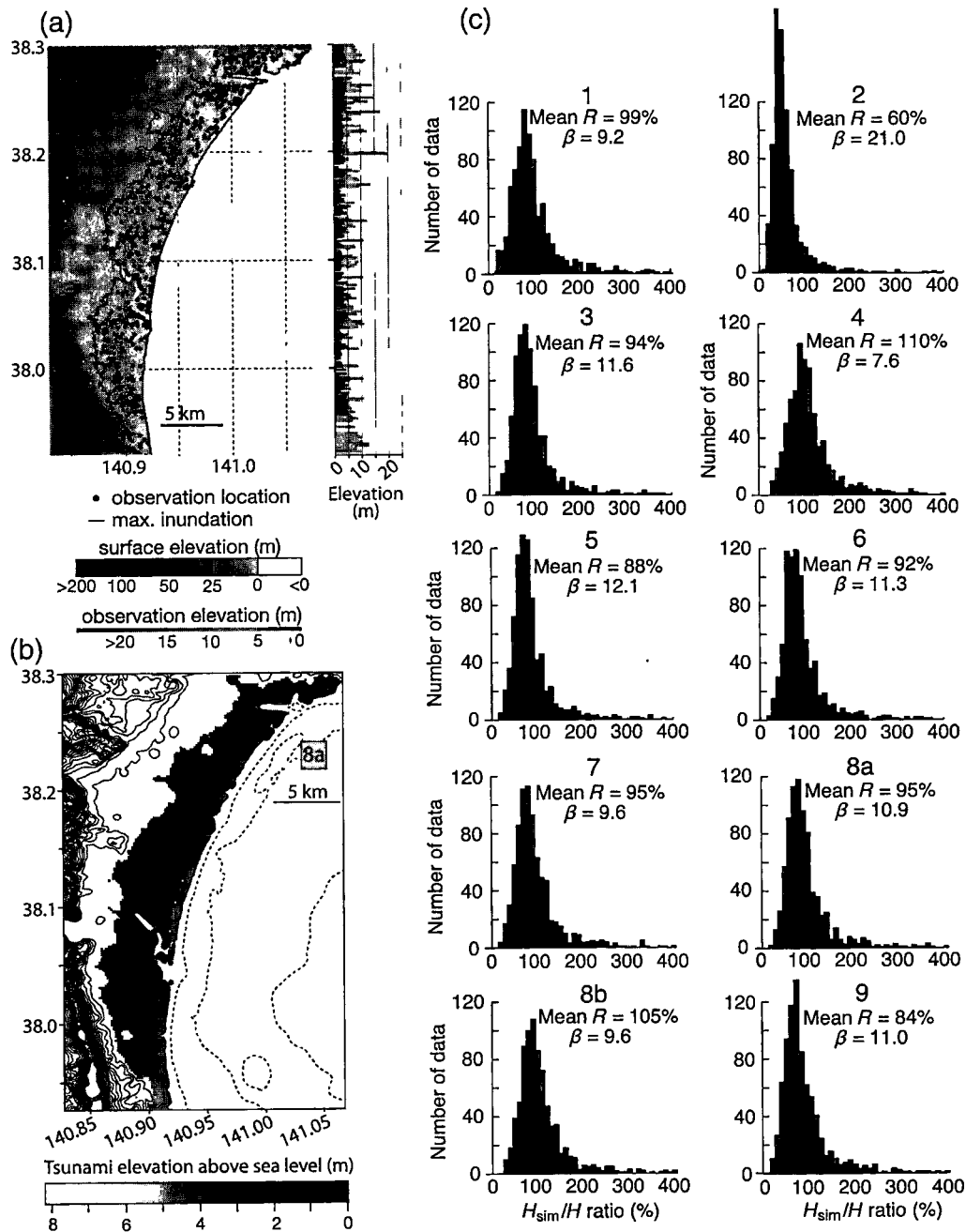


Figure 5. Sendai plain data and simulations. (a) Post-tsunami survey observations (dots and elevation graph) and inundation line from the Sendai plain; survey data from Mori *et al.*, 2012; inundation line based on survey data and satellite imagery. Observations less than 0 m were excluded from the data set. Topography is from the $3''$ grid used in simulation. (b) is an example of maximum simulated inundation (source 8a) that produced some of the best results for the Sendai plain. Contours are 10 m (dashed contours are below sea level). (c) Distribution of simulation wave heights divided by the observations shown in (a). Values $> 400\%$ are not included. $Mean R$ is the average ratio of H_{sim}/H ; β is the kurtosis of the distribution. The color version of this figure is available only in the electronic edition.

(2002). Cartesian grid cells in longitude–latitude are used, in which cell averages of the depth and momentum are approximated and updated in each time step. The method exactly conserves mass and also conserves momentum in regions where the bathymetry is flat. Inundation is handled by setting the depth in each grid cell to zero for dry land and positive for wet cells and allowing the state to change in each

time step. For more details about the algorithms, see the references cited previously.

Patch-based adaptive mesh refinement is used to place patches of refined grids on top of the coarse grid in regions for which a finer grid is needed. Several nested levels of grids are used, with refinement factors of four or more (in each spatial direction and in time) from each grid level to the next.

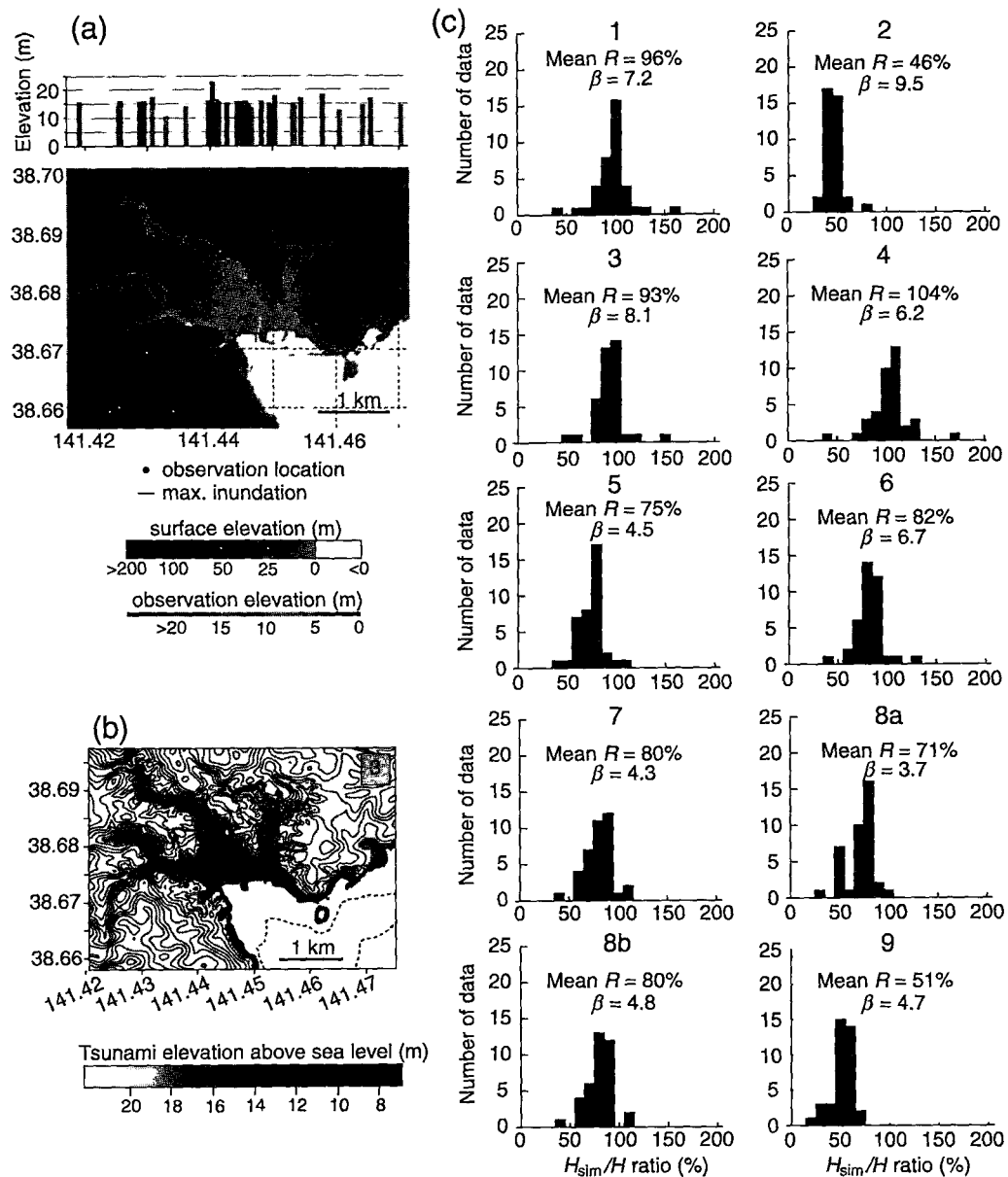


Figure 6. Shizugawa data and simulations. (a) Post-tsunami survey observations (dots and elevation graph) and inundation line in the Shizugawa district in Minamisanriku town; survey data from Mori *et al.*, 2012; inundation line based on survey data and satellite imagery. Topography is from the 1.3" grid used in simulation. (b) An example of maximum simulated inundation (source 3) that produced some of the best results for Shizugawa. Contours are 10 m (dashed contours are below sea level). (c) Distribution of simulation wave heights divided by the observations shown in (a). $Mean R$ is the average ratio of H_{sim}/H ; β is the kurtosis of the distribution. The color version of this figure is available only in the electronic edition.

Grids that follow the propagating tsunami across the ocean are dynamically determined based on flagging cells in which the surface displacement exceeds a threshold. Regions near the coastline for which inundation is modeled are typically refined to several additional levels, and the code allows the specification of more levels over specific regions in space-time.

In this study, grid resolution ranged between 2° and 0.2", with initial earthquake deformation files input at 4' resolution at the start of computation. Bathymetric grids used in Geo-

Claw simulations included 1' resolution grids obtained from ETOPO1 (Amante and Eakins, 2009) and coastal bathymetry with resolutions ranging from 0.2 to 3" created from bathymetric and topographic maps and satellite imagery. See Data and Resources for additional details. Refinement around the DART buoys ended at a final resolution of 5'. Inundation simulations of the tsunami were initially run along the entire Tohoku coastline at a low bathymetric resolution of 90". High-resolution inundation was run to 6" at the Sendai plain, to 0.2" at Taro, and to 1.3" at the other sites.

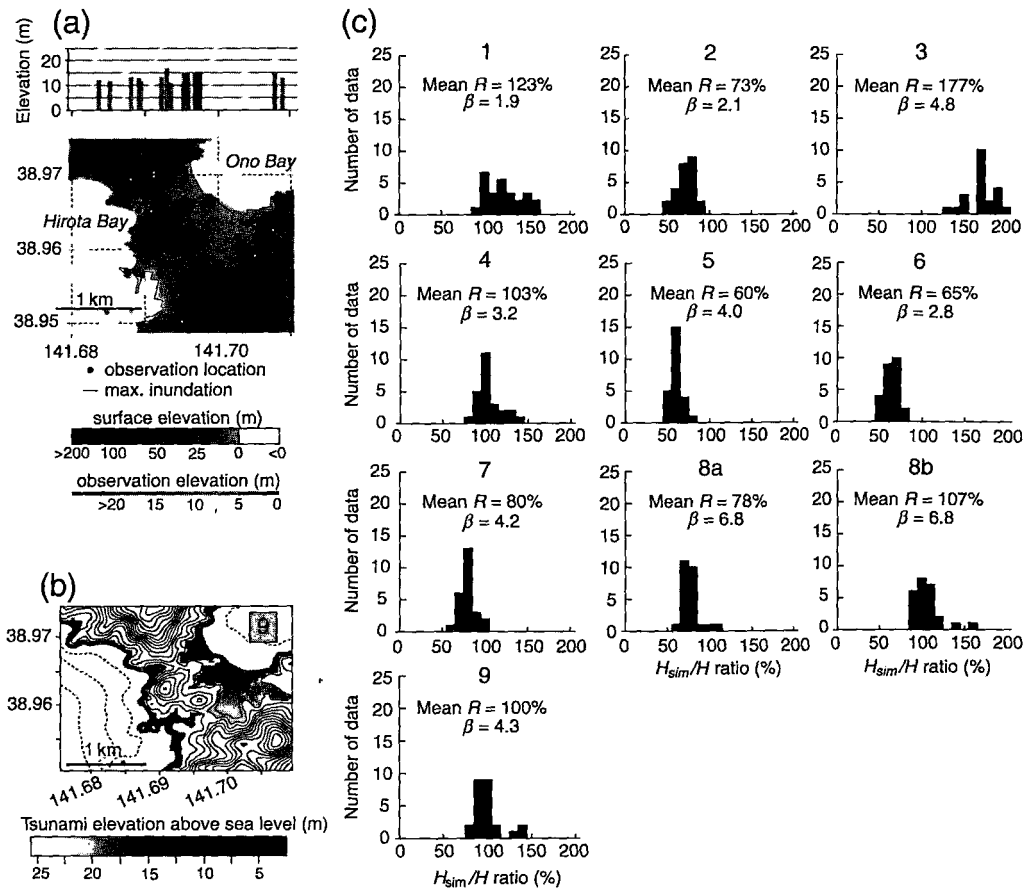


Figure 7. Hirota data and simulations. (a) Post-tsunami survey observations (dots and elevation graph) and inundation line near Hirota town in Rikuzentakata city; survey data from Mori *et al.*, 2012; inundation line based on survey data and satellite imagery. Topography is from the 1.3" grid used in simulation. (b) An example of maximum simulated inundation (source 9) that produced some of the best results for Hirota. Contours are 10 m (dashed contours are below sea level). (c) Distribution of simulation wave heights divided by the observations shown in (a). *Mean R* is the average ratio of H_{sim}/H ; β is the kurtosis of the distribution. The color version of this figure is available only in the electronic edition.

Higher bottom friction (0.035 rather than a standard 0.025 Manning's roughness coefficient) for the Sendai plain was warranted because of the 3–5-km-long inundation distance over rice paddies; 0.035 is considered an appropriate Manning's roughness coefficient for pasture and farmland. Reasonable friction terms were tested in other sites with results of up to a few meters difference in simulated tsunami heights, but without apparent improvement of simulations versus observations.

Seafloor Deformation from Selected Earthquake-Slip Distributions

Simulation runs in this study use instantaneous sea-surface deformation as the initial condition at $t = 0$. For sources 7, 8b, and 9, the sea-surface-deformation fields were provided by the authors of previous studies (Saito *et al.*, 2011; Gusman *et al.*, 2012; Tang *et al.*, 2012; Wei *et al.*, 2012). For other simulations, we computed the sea-surface deformation from heterogeneous fault models available in previous studies (Ammon *et al.*, 2011; Fujii *et al.*, 2011;

Hayes, 2011; Shao *et al.*, 2011; S. Wei *et al.*, 2011; Gusman *et al.*, 2012) and from a single fault model based on the GCMT solution (M_w 9.1). The initial sea-surface deformation is assumed to be equal to the coseismic deformation of the seafloor. The deformation of the seafloor is computed for each subfault using Okada (1985) equations. Results can be seen in Figure 2. For dynamic fault models, that is, those in which the rupture process was of finite duration, the final seafloor displacement was used, and assumed to occur instantaneously. This is discussed further in the next section.

Comparisons of Simulations and DART Records

We used data from DART buoys 21401, 21413, 21418, and 21419 to test how well the simulation for each source model matches the tsunami waveform at locations away from the coast. A detiding algorithm was applied to the data set for each buoy from 11–15 March to obtain a set of data points at discrete times (after replacing a few obvious isolated bad data points by interpolated values). The detiding was performed by least-squares fit of a polynomial of degree 15

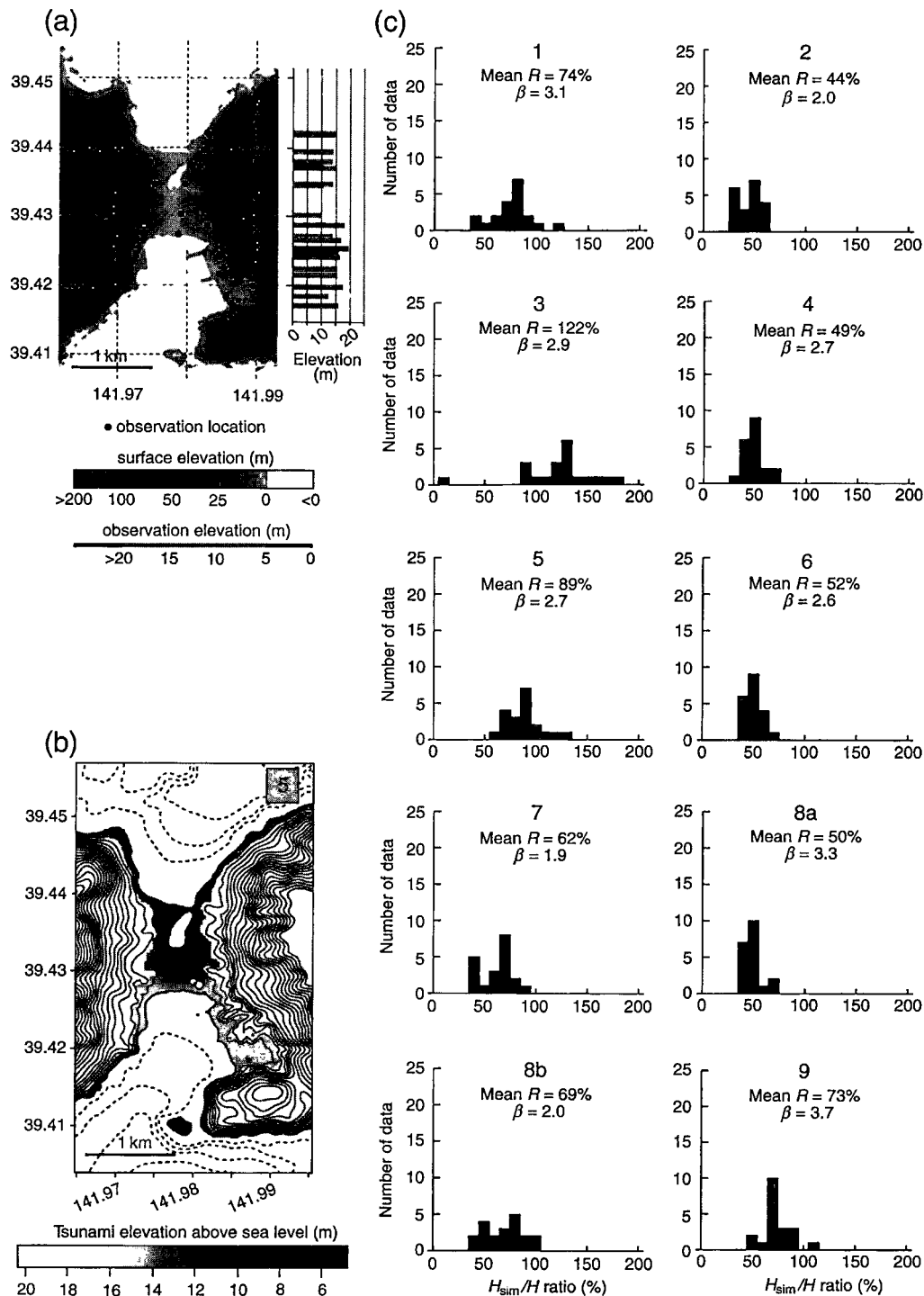


Figure 8. Funakoshi data and simulations. (a) Post-tsunami survey observations (dots and elevation graph) for the Funakoshi district in Yamada town; survey data from Mori *et al.*, 2012. Topography is from the 1.3" grid used in simulation. (b) An example of maximum simulated inundation (source 5) that produced some of the best results for Funakoshi. Contours are 10 m (dashed contours are below sea level). (c) Distribution of simulation wave heights divided by the observations shown in (a). $Mean R$ is the average ratio of H_{sim}/H ; β is the kurtosis of the distribution. The color version of this figure is available only in the electronic edition.

to a 48-hr window of data around the tsunami arrival time. The time interval between data points collected by the DART varies from 15 min when no event was detected to 1 min or 15 s (for the initial few minutes) during the event; $\text{\textcircled{E}}$ the raw data and detiding code is available in the electronic supple-

ment to this paper. In order to have a uniform set of times for estimating the difference between simulated and observed waveforms, a piecewise linear function $G(t)$ was defined by the data set, and was sampled at 15-s intervals over a time period of 2 hrs starting just before the tsunami arrived at the

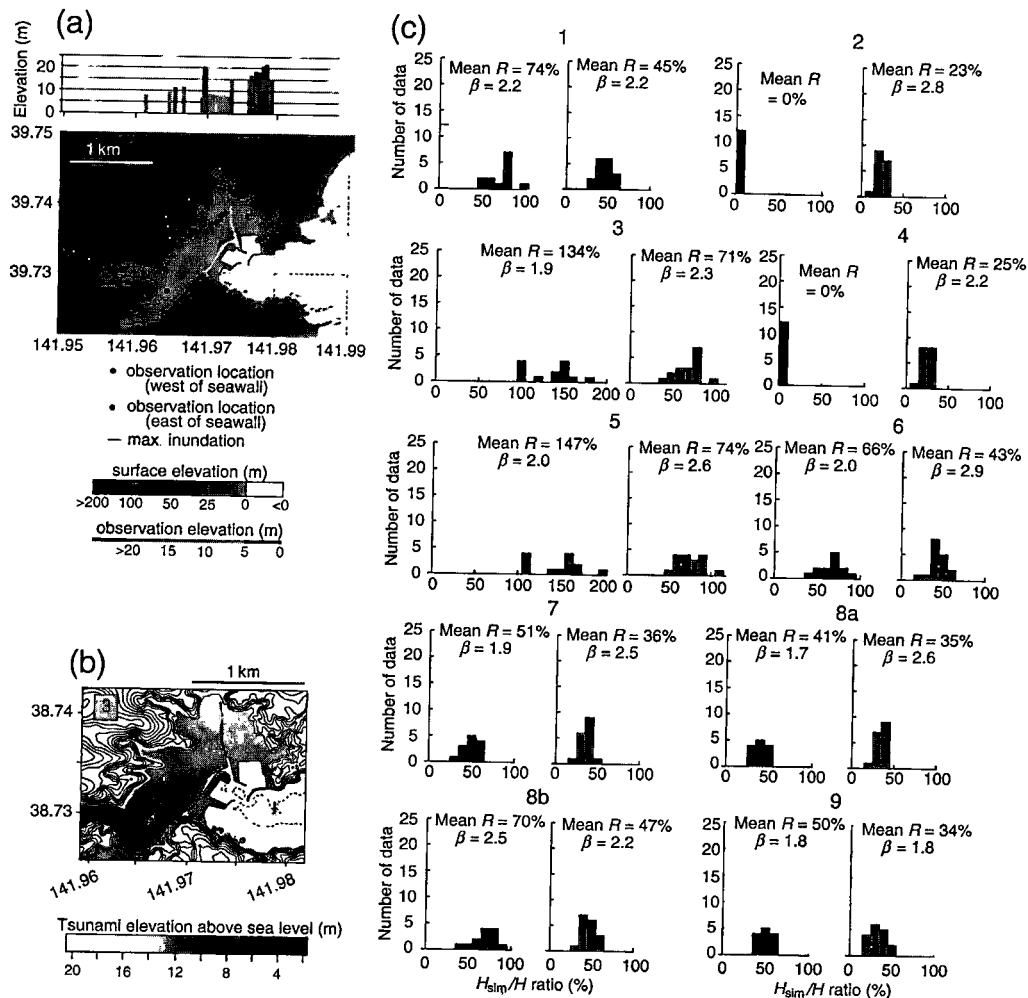


Figure 9. Taro data and simulations. (a) Post-tsunami survey observations (dots and elevation graph) and inundation line in the Taro district in Miyako city; survey data from Mori *et al.*, 2012; inundation line based on survey data and satellite imagery. Topography is from the 0.2" grid used in simulation. (b) An example of maximum simulated inundation (source 3). Contours are 10 m (dashed contours are below sea level). (c) Distribution of simulation wave heights divided by the observations shown in (a). *Mean R* is the average ratio of H_{sim}/H ; β is the kurtosis of the distribution. Results are divided into west (dark shade) of the seawall and east (light shade) of the seawall. The color version of this figure is available only in the electronic edition.

gauge. From each simulation, numerical data was computed at each DART location at each time step. A piecewise linear function $S(t)$ is defined by the simulation data and was sampled at the same 15-s intervals as used for the DART data. Times are reported (in s) relative to the initiation of the earthquake at 5:46:24 UTC on 11 March 2011. Although this start-time value is consistent with those sources for which the inversion assumed instantaneous rupture, it may not be optimal for sources associated with inversions that assume dynamic ruptures. When replacing dynamic with instantaneous rupture, it would make more sense to choose a time partway through the rupture process rather than initiate deformation at $t = 0$. This is equivalent to choosing a displacement time T_d and computing the root mean square (rms) of residuals based on the discrepancies $G(t_j) - S(t_j - T_d)$ for which $t_j = t_0 + 15j$ for $j = 1, 2, \dots, 480$ are the times at 15-s increments over 2 hrs, starting at some time

t_0 just before the tsunami arrived, and the rms is the square root of the sum of the squares of these discrepancies. Changing T_d (and hence shifting the peaks) can make a large difference in the size of the discrepancy at the discrete times and hence the residual. However, because it is not clear what value of T_d should be used for each model, we allow T_d to be a free parameter and choose T_d for each combination of simulation and observation to minimize the resulting rms of residuals (Table 2). Results are presented and discussed subsequently. Shifted waveforms can be found in Figure 3 and are plotted next to unshifted waveforms in (E) Figure S1 (see electronic supplement).

Comparisons of Simulations and Onshore Records

Researchers from throughout Japan and the world participated in the 2011 Tohoku earthquake–tsunami joint survey groups, conducting a tsunami survey along a 2000-km

Table 1
Overview of the 2011 Tohoku Earthquake Sources Used in This Study

Simulation ID		1	2	3	4	5	6	7	8a	8b	9
Citation	(GCMT solution)	Hayes (2011)	Shao <i>et al.</i> (2011)	Ammon <i>et al.</i> (2011)	S. Wei <i>et al.</i> (2011)	Fujii <i>et al.</i> (2011)	Saito <i>et al.</i> (2011)	Gusman <i>et al.</i> (2012)	Tang <i>et al.</i> (2012) and Wei <i>et al.</i> (2012)		
Inversion Methodology	n/a	Seismic Inversion	Seismic Inversion	Seismic and GPS Inversion	Seismic and GPS Inversion	Tsunami Inversion	Tsunami Inversion	Tsunami and GPS Inversion	Tsunami Inversion		
Earthquake parameters	M_0 (N·m)	5.3×10^{22}	4.9×10^{22}	5.75×10^{22}	3.6×10^{22}	4.7×10^{22}	3.8×10^{22}	—	4.0×10^{22}	5.1×10^{23}	1.6×10^{22}
	M_w *	9.15	9.13	9.17	9.04	9.16	9.05	9.0	9.07	9.14	8.84
	Number of subfaults	1	325	190	560	350	40	130	45		6
	Subfault size (length \times width, km)	300×150	25×20	25×20	15×15	25×20	50×50	43.1×24	50×40	100×50	
Timing	Duration of rupture (s)	Instantaneous	244	177	232	Instantaneous	Instantaneous	Instantaneous	Instantaneous		Instantaneous
	Subfault rise time (s)	0	7.6–26.4	1.6–16	20–40	0	30	0	0		0
Sea surface deformation	Tsunami model	—	—	—	—	—	Shallow-water wave equations (Satake, 1995)	Shallow-water wave equations with dispersion (Saito <i>et al.</i> , 2010)	Shallow-water wave equations (Johnson, 1998)		Shallow-water wave equations (Titov and Synolakis, 1998)
	Equations for relating sea surface deformation to slip	—	—	—	—	—	Okada (1985) and Tanioka and Satake (1996)	Slip not calculated	Okada (1985) and Kajura (1963)		Gusiakov (1978)

*Assuming a shear modulus of 4.0 GPa.

stretch of the Japanese coast (Mori *et al.*, 2012). They measured more than 5200 points of tsunami height within the inundation area and runup height at the limit of inundation (Fig. 4, upper left); the surveyors corrected these data for tides. We used their data for comparison with simulated tsunamis to evaluate the performance of each source model in reproducing the actual tsunami heights. This was done all along the coast at a fairly low resolution and runup was estimated by first determining which grid cells are shoreline cells (wet cells with dry neighbors or vice versa). The maximum surface elevation in each cell was monitored throughout the simulation and then the maximum in each shoreline cell was plotted against the latitude of the cell center to produce the plots in Figure 4. Large-scale versions may be found in [Ⓔ](#) Figure S13 (see electronic supplement) and the data sets are also available in [Ⓔ](#) the electronic supplement.

At five sites along the coast, high-resolution runs were used to simulate more detailed inundation. For each post-tsunami observation at each of these sites, the maximum height above sea level of the tsunami simulation (H_{sim}) was compared to the actual measurement (H) at the same position, or the closest inundated point when simulated inundation fell short of observations (Figs. 5–9). The rms of residuals between H_{sim} and H was calculated for each site (Table 2). In addition, the ratios between simulated and observed tsunami heights (H_{sim}/H) at each site are plotted in a

histogram with intervals of 10% (Figs. 5–9). The kurtosis (β) of the ratio distribution shows how well the simulation produced the overall observed pattern of inundation. The more peaked and narrow the histogram, or larger the kurtosis value, the better the simulation was able to represent the pattern of observations (Figs. 5–9). The K factor from Aida (1978), an additional comparison method for tsunami simulations and observations, can be found in [Ⓔ](#) Figure S2 (see electronic supplement). All simulated inundation maps and point comparisons are also in [Ⓔ](#) Figures S3–S12 (see electronic supplement).

Results

Characteristics of Seafloor Deformation

For most of the sources used in this study, maximum uplift of the calculated seafloor deformation (ranging from 7 to 20 m) was near the trench and centered around 38° N ($\pm 0.5^\circ$), 143.25° E ($\pm 0.75^\circ$; Fig. 2). Deformation from sources 1, 4, 5, and 9 deviate slightly from this commonality; maximum uplift was more southern and western in source 4, was more northern in 9, and was more widely distributed in 1 and 5. Source 2 produced an additional area of uplift near the epicenter and 5 produced more uplift off central Iwate than others. Compared to uplift, coseismic subsidence was more

Table 2

rms of Residuals between Simulated Tsunami and Observed Waveforms at DART Buoys or Tsunami Heights on Land. Also Reported are the Offset Time (T_d) that Optimizes the rms between Simulated and Observed DART Wave Forms and the Arrival Time of Simulated Tsunamis at the Sendai Airport

		1	2	3	4	5	6	7	8a	8b	9
	Location	Uniform Displacement	Seismic Inversion	Seismic Inversion	Seismic and GPS Inversion	Seismic and GPS Inversion	Tsunami Inversion	Tsunami Inversion	Tsunami and GPS Inversion	Tsunami Inversion	
Unshifted waveforms*	21418(6.77)	5.35	6.04	9.05	5.43	5.26	3.33	4.47	4.43	5.28	6.01
	21401(3.20)	2.49	2.77	3.43	2.42	3.41	1.25	1.31	1.66	2.05	1.79
	21419(2.73)	2.30	2.21	2.83	2.08	2.65	1.27	1.13	1.54	1.81	1.56
	21413(3.94)	3.51	2.95	5.14	2.58	3.79	2.48	2.64	3.06	4.53	4.03
Waveforms shifted by T_d *	21418(6.77)	5.31	4.15	6.34	4.70	3.99	2.91	2.87	3.72	4.05	3.36
	21401(3.20)	2.35	2.03	1.50	2.14	1.92	1.19	1.16	1.12	1.39	1.69
	21419(2.73)	2.18	1.73	1.11	1.89	1.69	1.11	0.87	0.92	1.11	1.36
	21413(3.94)	3.05	1.94	2.44	2.45	1.87	1.37	1.12	1.60	2.47	2.25
T_d (s)	21418	-38	119	178	-113	117	37	90	90	111	134
	21401	111	291	247	-159	425	27	53	111	115	50
	21419	146	334	255	-158	433	53	75	145	138	71
	21413	102	165	244	40	292	113	154	146	185	193
Inundation simulation	Sendai Plain	2.49	3.34	2.44	2.24	2.60	2.49	2.53	2.44	2.25	2.80
	Shiaigawa	3.33	8.79	3.20	3.38	5.07	4.36	4.48	5.64	4.55	8.08
	Hirota	4.00	3.78	9.61	1.98	5.04	4.63	2.78	3.04	1.99	2.12
	Funakoshi	4.75	8.35	5.50	7.64	2.78	7.26	5.89	7.62	5.20	4.51
	Taro west	3.38	9.93	3.53	9.93	4.46	3.95	5.09	6.12	3.55	5.20
	Taro east	10.88	14.48	6.88	14.16	6.40	11.20	12.33	12.52	10.68	12.59
Arrival time, Sendai airport (min. post earthquake)		67.5	73.8	72.0	61.8	72.5	66.9	70.6	68.8	68.8	72.2

*rms of residuals of no simulated wave (flat water) in parentheses.

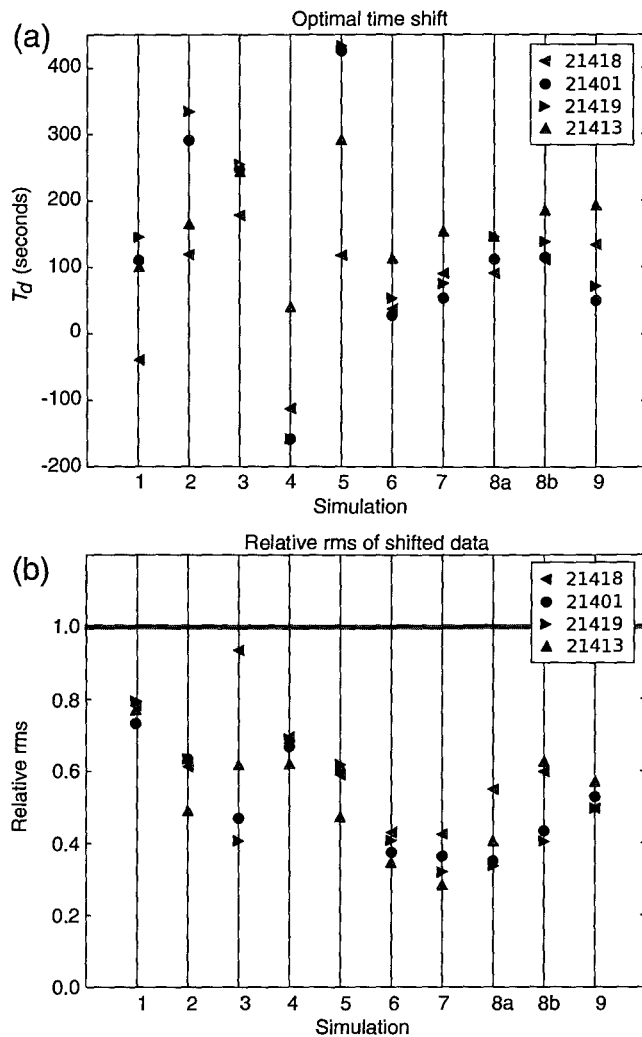


Figure 10. (a) The optimal number of seconds (T_d) the waveform should be shifted in time to minimize the rms of residuals between simulations and observations at each DART. (b) The relative rms, defined as the rms of residuals between each simulation and DART observation normalized relative to the rms of residuals for the DART compared to flat water (see Table 2), using the T_d time shifts in (a). The color version of this figure is available only in the electronic edition.

variably located, though it spanned a smaller range of values, from -2 to -7 m. Many sources predict subsidence in Tohoku greater than 1 m (1, 4, 5, 6, and to a small degree, 8a, and 8b), especially near Oshika Peninsula (at 38.3° N).

Characteristics of the Tsunami

DARTs. Figure 3 shows the simulated DART results after shifting each by an optimal time shift T_d as discussed above (the unshifted results are shown in $\textcircled{\text{E}}$ Fig. S1, electronic supplement). Table 2 shows the rms of residuals between simulated and observed tsunami waveforms computed at each DART buoy using each source, along with the optimal time shift T_d used for each. Also listed in parentheses is the rms of residuals computed using $S(t) = 0$, that is, using flat water

(undisturbed ocean with no waveform present) in place of the tsunami simulation results, to provide a scale for judging the magnitude of the rms. The ratio of the two, defined as the relative rms, is plotted in Figure 10 to aid in comparing results between different DART locations. The optimal T_d for sources 3 and 6–9 all were roughly the same when computed from any DART location, whereas the other sources gave more scattered values of T_d (Fig. 10). Ideally, the T_d value from any one source would be similar for each DART waveform, although when a dynamic fault-rupture model is replaced by instantaneous displacement, it may not be surprising that different times are optimal in different directions from the fault. What is more surprising is that the optimal T_d often lies outside the interval from 0 to 60 s when most of the rupture occurs.

The rms of residuals does not tell the entire story, and it is important to also compare waveforms visually. DART 21418 is closest to the epicenter and from Figure 3 we see that sources 3, 7, and 8b do the best job of predicting the peak magnitude at this point. DART 21401 and 21419 are close to each other northeast of the epicenter. Again sources 3, 6, and 8b best reproduce the leading wave. DART 21413 is southeast of the epicenter and here sources 3, 4, and 8b significantly overpredict the leading peak, whereas 1, 7, 8a, and 9 do the best job.

Tohoku Near-Field Runup (Low-Resolution Simulations).

In most places, tsunami simulations resolved to $90''$ underestimate observations. Simulations also do not produce the pattern of maximum observed runup (an average of 10–20 m) between $\sim 39^\circ$ and 40° N (Fig. 4). Instead, highest simulated runup occurs just north of 38.3° N. Only simulation 3 and possibly 8b give many results larger than observations in Tohoku in these low-resolution runs (Fig. 4). Simulations 3 and 5 produce the highest tsunami between 39° and 40° N, although they still underestimate many of observation data points in this region. The main differences between simulations occur either from 37° to 38° N, for which simulations 3, 4, 8a, and 8b produce runup over 10 m whereas other simulations do not, or north of 38.3° N, for which the zone of values higher than 10 m extends to $\sim 39.5^\circ$ N (simulations 1, 3, 5, 8b, and 9) or only to 39° N (simulations 2, 4, 6, 7, and 8a).

Sendai Plain. Almost all simulations give good results at the Sendai plain; the mean H_{sim}/H ratios for most simulations are very close to 100% (Fig. 5). Only the tsunami from source 2 is distinctly too small. The kurtosis of the ratio distribution of simulation 4 is the lowest, indicating it produced a poorer match with the overall pattern of observations. For the remaining simulations, neither the mean H_{sim}/H ratio nor the kurtosis of that ratio can clearly differentiate the simulation best able to reproduce observations. Sources 1, 7, 8a, and 8b all average within 5% of a 100% mean H_{sim}/H ratio, whereas simulations 3, 5, and 6 have slightly higher kurtosis values. The arrival time of the main tsunami inundation (71 min after rupture) at the Sendai airport is close to the

observed time in most simulations, although simulation 4 is too early by ~ 10 min whereas 2, 3, 5, and 9 are slightly late (see Table 2).

Shizugawa. Simulations 1, 3, and 4 have the closest mean H_{sim}/H ratio to 100%, simulations 2 and 9 produce small mean ratios of about 50%, whereas other simulations slightly underestimate observations in Shizugawa district of Minami-sanriku town (Fig. 6). Kurtosis of the H_{sim}/H ratio distribution suggests that simulation 3 matches the overall pattern of runup better than simulations 1 or 4; further analysis of the simulated inundation maps show that simulation 4 is too large in the western river valley in Shizugawa (see Fig. S5, see electronic supplement).

The coseismic subsidence produced by the sources is highly variable at Shizugawa (Fig. 2). The seafloor deformation pattern of source 4 results in 2 m of subsidence and that of 3, 5, and 6 results in subsidence between 1 and 2 m. GPS receivers in the area recorded 0.66 m of subsidence, similar to values calculated from source models 1, 8a, and 8b.

Hirota. Simulations 4, 8b, and 9 clearly have the closest mean H_{sim}/H ratio to 100%. Simulation 3 significantly overestimates observations, by 10 m in many cases. Simulation 1 is also too large, whereas most other simulations are 20%–40% too small (Fig. 7; Table 2). Simulations 5 and 6 produce the smallest tsunamis. Kurtosis of the H_{sim}/H distribution suggests that simulation 8b better produced the overall pattern of observations than either 4 or 9, although all three cases produce a wave too high near the eastern shore (see Fig. S8, electronic supplement). Inundation maps (see Fig. S7, electronic supplement) show that most simulations yield a larger wave in Ono Bay (northeast) than Hirota Bay (southwest), as was observed. The tsunamis in simulations 4 and 8b cross the isthmus between the two bayside areas (as do 1 and 3), an event which did not occur, whereas simulation 9 more closely matches the inundation limit.

Funakoshi. All simulations underestimate observations in Funakoshi, with small mean H_{sim}/H ratios. Simulations 3 and 5 are the closest to 100%, but the distributions of the ratio from those simulations have small kurtosis values, which indicate that they do not reproduce the overall pattern of observations (Fig. 8). Simulation 9 slightly underestimates the observations with a mean ratio of 73% and with the largest kurtosis of the ratio distribution (Fig. 8). Other simulations yield either smaller mean ratio or smaller kurtosis. All simulations result in a higher tsunami at the south end of the Funakoshi isthmus than in the north (see Fig. S9, electronic supplement), as was observed.

Taro. Many simulations clearly overtop the seawalls in Taro, whereas simulations 2 and 4 did not (Fig. 9). No simulation results in a good match with the observed pattern of a 15–20-m-high tsunami on the seaward (east) side of the seawalls and an 8–15-m-high wave on the landward (west) side.

At best, simulations that overtop the wall result in only a few meters difference in the elevation of the tsunami between the two sides at observation locations (see Fig. S12, electronic supplement). Many simulations are too small on the east side, although 3 and 5 produce the best agreement because they create the largest tsunami in general in Taro. However, these two simulations are too large on the west; inundation maps clearly show that simulations 3 and 5 penetrate farther inland than the mapped inundation line (see Fig. S11, electronic supplement). The underestimating simulations 1 and 8b and the overestimating simulation 3 yield the closest agreements with observations on the west side, with the closest mean H_{sim}/H ratio to 100% (Fig. 9; Table 2).

Discussion

Tsunami Simulations at DART Buoys

Tsunami inversions, especially 6, 7, and 8a, recreate open-ocean measurements more closely than many seismic inversions, based on rms results (Table 2; Fig. 10). Although expected, this has not always been the case in previous studies, such as from the 2004 Indian Ocean event, for which seismic and GPS inversions better recreated sea-surface anomalies measured by the Jason-1 satellite than tsunami inversions (Poisson *et al.*, 2011). In the 2011 Tohoku example, tsunami inversions used DART waveforms as input data in their calculations, allowing these sources to better reproduce that same waveform data, in spite of the fact that they used a different tsunami model and often a different method to calculate sea-surface deformation than the methods used in our study. Results from source 1 clearly indicate that all sources derived from slip inversions are better able to match observations than the uniform-slip source (Fig. 10b).

In past examples, timing has been shown to have significant impact on the tsunami waveform for long-duration ruptures (Pietrzak *et al.*, 2007; Poisson *et al.*, 2011). Although we have not included rupture timing in this study, the optimal shift (T_d) of DART waveforms potentially indicates that including rise time or rupture propagation could result in a better fit with the data. For example, the T_d for 3 of 4 cases is 30–60 s for simulation 6 (Table 2), similar to the 30-s rise time used in that inversion. Also, simulation 4 shows a progressively later T_d from north to south, possibly correlating with rupture propagation.

Tsunami Inundation South of 39° N

Tsunami simulations were generally good at producing inundation similar to observations in the Sendai plain and the Sanriku coast south of 39° N. However, the best fitting simulations on land are different than those at the DART buoys. Simulation 4 is one of the best simulations at the Sendai plain, Shizugawa and Hirota, followed by 8b and 3. Wei, Titov, Newman, *et al.* (2011) obtained similar inundation results as our study in the Sendai plain, with source 9 giving

better results than 2. Grilli *et al.* (2012) found that source 3 significantly overestimated results just north of 38.3° N; we obtained similar results in this region in our coarse-resolution runs.

In contrast to the coarser-resolution runs, when simulation 3 was refined to a higher resolution in Shizugawa, the wave heights were smaller and therefore more accurate. Tsunami heights between simulations at 90" resolution vary by as much as 10 m (Fig. 4), but after refinement to 1.3" the variation decreased to ~5 m with smaller simulations amplifying and larger simulations being reduced in height. This suggests that tsunami models run only on a relatively coarse grid can overestimate the variability of the tsunami.

Simulations from the Sendai plain are virtually indistinguishable based solely on comparisons at observation locations. The implications of a congruence of most results in the Sendai plain are that the choice of a source model in any future impact studies may be of less importance in this location. The relatively simple and smooth Sendai coastline, combined with the broad shelf offshore, may transform incident tsunamis in a way that reduces their differences, resulting in tsunami inundation that gives very similar tsunami heights. However, except for noting tsunami arrival times at the Sendai airport, the temporal evolution of detailed flow dynamics were not investigated in this study, and this aspect of the event may be important to consider in future studies.

Tsunami Inundation North of 39° N

In this study, all simulations at 90" resolution underestimate observations north of 39° N (Fig. 4), and most simulations at 1.3" resolution also underestimate tsunami observation in Funakoshi and Taro (39.43° and 39.73° N, respectively). Based on past research, the coarse-resolution simulations were not expected to accurately reproduce the distribution of tsunami wave heights observed along the Sanriku coast, and this is borne out by the results presented in Figure 4. Previous simulations of the 2011 Tohoku tsunami at relatively coarse resolutions have noted that the inundation of central Iwate prefecture (~39° to 40.5° N) is underestimated in a way that is similar to our results, for example, Grilli *et al.* (2012) using source 3 and Wei, Titov, Newman, *et al.* (2011) using sources 2 and 9. Inaccurate or poorly refined bathymetry can cause reflections and focusing of the wave to be erroneously enhanced or ignored and the underestimation from 39° to 40° N is often cited as being a result of challenges with bathymetric accuracy and resolution (Wei, Titov, Newman, *et al.*, 2011; Grilli *et al.*, 2012; Yim *et al.*, 2012). Yim *et al.* (2012), using a source by Yamazaki *et al.* (2011), show relatively good agreement with offshore GPS buoys, but still underestimate the wave at inundation locations; they cite the differences as due to the coarse (20") resolution bathymetry. Because the GPS buoys are in 100–300-m water depth, the wave is less affected by bathymetry and thus the deeper water results could be more accurate than those on land. Moreover, simulations at 2' resolution by

Wei, Titov, Tang, *et al.* (2011) were unable to produce the higher runup values, whereas finer simulations at 3" resolution resulted in significantly better agreement with coastal observations. Shimozono *et al.* (2012), using 50-m resolution, calculated very good agreement between simulated and observed tsunami heights, with the exception of a handful of cases in which the topographic slope was steeper than 0.030 and the tsunami was greater than 25 m. Higher resolution bathymetry and computational grids are therefore necessary when simulating complex topography.

In our high-resolution simulations, two sources overestimate results in parts of central Iwate: simulation 3, which is too large in both Funakoshi and western Taro, and simulation 5, which is too large in western Taro. Simulation 3 produces the largest amplitude wave during propagation across the Japan shelf, including generating the greatest heights off northern Miyagi prefecture (38.3–39° N) of any simulation, whereas simulation 5 is the only simulation in coarse-resolution runs to have higher runup values at 39.5° N than 39° N. Because two inversions result in a tsunami larger than observations in high-resolution computations of Funakoshi and western Taro, the tendency to underestimate the wave in central Iwate is more likely due to a missing secondary source rather than significant bathymetric problems with our grids. Shimozono *et al.* (2012) also simulated Funakoshi using only the GPS buoy data from offshore central Iwate as a boundary condition, as opposed to an earthquake source; their results produced better agreement with observations than any of our sources. Four of the tsunami inversions (6, 7, 8a, and 8b) in this study also use the same GPS buoys in their inversions. However, comparisons of observations with the synthetic waveforms of their inversions (Fujii *et al.*, 2011; Saito *et al.*, 2011; Gusman *et al.*, 2012) show that the synthetic waveforms underestimated the tsunami in central Iwate, therefore underestimation was incorporated into their solutions. Consequently, it is likely that a secondary source, local to offshore central Iwate and therefore not captured by tsunami inversions incorporating many more data than just the central Iwate records, was responsible for a component of the higher tsunami in central Iwate. If this secondary source occurred within or close to the time frame of the main rupture or was localized to the Iwate prefecture, such as a splay-fault rupture, landslide, or aftershock, it could be overlooked by many or all of the earthquake source inversions. Splay faults likely ruptured coseismically with the main event (Tsuji *et al.*, 2011), although a splay-fault rupture would need to be fairly localized to not be recorded by the dense network of GPS receivers or seismometers in Japan. Submarine landslides have been observed in the Japan trench (Kawamura *et al.*, 2012), but a local landslide near central Iwate, such as along the continental shelf edge, could have occurred as well. Potentially, lateral movement of bathymetric features during the earthquake (Tanioka and Satake, 1996) could be an overlooked source for the initial tsunami as well.

Does Any One Source Match Tsunami Observations Better?

Which source can produce the most accurate simulation of the 2011 Tohoku tsunami everywhere could not be determined using only the four DART buoys and the five locations with high-resolution bathymetry used in this study due to the complexity and variability of the tsunami along the coast. Simply adding the rms values from the DARTs and high-resolution simulations in Table 2 suggests that sources 1, 3, 7, and 8b produced some of the best results based on their lower sum total rms of residuals. Although these sources do better in our areas of interest, these areas do not give a full picture. For example, as noted earlier, source 3 was too large in southern Sanriku. However, many conclusions can be made using the locations simulated in this study. Source 4 gave good results south of 39° N, whereas source 2 was consistently too small. Only source 5, the source with the most spatially extensive northern rupture, had a better fit with the data north of 39° N (at Funakoshi and Taro) than south, supporting the interpretation that an additional source of deformation needs to be included in most inversions for them to produce tsunami observations north of 39° N. That uniform slip from source 1 resulted in one of the better simulations at many high-resolution sites is encouraging for future work with real-time or rapid-assessment tsunami models. Similar results for the best earthquake sources for simulating the near-field tsunami are expected for other tsunami models besides GeoClaw, as long as high-resolution bathymetry is used in simulation.

Limitations of Our Methods

We have used only instantaneous seafloor displacement, even for sources for which dynamic rupture information is included. The GeoClaw code can use dynamic rupture information but preliminary investigation with source 3 shows that this makes little difference. When comparing time-shifted DART results, we felt it was best to use the same procedure for all sources. Moreover, most tsunami models use instantaneous displacement and our goal in part is to determine which sources are best to use for other modelers as well.

The GeoClaw code solves the shallow-water equations with no dispersive terms. For long waves this is generally accurate, but during the initial phase of tsunami generation a sharp peak in the seafloor displacement could produce dispersive waves. At DART 21418, closest to the epicenter, high-frequency oscillations in the observed data are not matched by any of our simulations. Saito *et al.* (2011) point out that these oscillations can be captured with dispersive equations.

Tsunami observations show that the actual tsunami often has localized higher values of tsunami height or runup. Even with reasonably high-resolution bathymetry and topography, tsunami simulation of onshore records cannot capture the small-scale variability in height of the actual wave. For example, simulations that overtop the seawall in Taro did not reproduce the pattern of larger tsunami heights in eastern

Taro than that in western Taro. This may indicate that GeoClaw did not capture necessary physical processes that occurred during inundation there. In videos of the tsunami in Taro, the tsunami's interaction with the seawall does not have a noticeable effect on the water's seaward elevation, with the exception of a standing wave and hydraulic jump that develops at the wall. However, the tsunami can be seen locally increasing its height after encountering large buildings, buildings which are not included in the model. There is also an abundance of large debris in the water, most notably cars and shipping containers from the port that could have dammed the flow, with decreasing regularity away from the port.

Conclusions

Slip distributions of the 2011 Tohoku earthquake obtained by previous studies result in distinguishable near-field tsunamis. The choice of slip distribution affects tsunami waveforms, runup heights, and arrival times of simulated tsunamis and therefore should be considered to optimize results in future studies. Simulations using high-resolution bathymetry are needed to determine detailed results of possible wave behavior and accurate tsunami heights during inundation; most simulations on low-resolution bathymetry underestimate the tsunami. There is no discernible pattern as to whether the wave was amplified or dampened in low-resolution compared with high-resolution runs, supporting the idea that bathymetry plays a significant role in controlling the process of inundation and determining final wave heights on land. Many sources produced realistic inundation in the Sendai plain in both high- and low-resolution simulations. At the Sendai plain, differences between the sources simulated in this study seem to be the result of bathymetric effects during propagation and inundation in this region. Source selection for future work along the Sendai plain does not need to be as discerning as along other coastal areas in Japan.

Combined results of all earthquake inversions suggest that an additional source of tsunamigenic energy is needed to explain observations of tsunami runup in central Iwate prefecture (39°–40° N), a result similar to other tsunami-simulation studies. Coseismic rupture of local splay faults, seismically induced landslides, and lateral motion of the coastline and/or bathymetric features are a few mechanisms that might have generated additional tsunami waves.

Many simulations give good inundation results using high-resolution bathymetry. Tsunami inversions generally recreate open-ocean measurements at DART buoys more closely than many seismic inversions, although that trend does not extend to onshore sites. In Tohoku, many inversions produce results within 20% difference from the observations between 38° and 39° N, potentially reflecting a reliance on a large initial seafloor uplift around 38° N ($\pm 0.5^\circ$), 143.25° E ($\pm 0.75^\circ$) to create the observed pattern of runup in that region. Our modeling efforts of the near field of the 2011 Tohoku earthquake shows that it is necessary to test multiple

earthquake-source models before choosing the source best able to produce observations for further investigations.

Data and Resources

Tsunami Model

GeoClaw is an open source code available at <http://www.clawpack.org/geoclaw/> (last accessed March 2012). GeoClaw Version 4.6.1 was used in this study.

Bathymetry Data

The bathymetry data sets used for tsunami simulation are based upon ETOPO1 (Amante and Eakins, 2009), Japan Hydrographic Association's M7005 bathymetric contour data, Advanced Spaceborne Thermal Emission and Reflection Radiometer (ASTER) Global Digital Elevation Model (GDEM), and Geospatial Information Authority of Japan (GSI) topographic contour maps. ETOPO1 and ASTER GDEM both use generic mean sea level as their vertical datum. The GSI topographic maps use the Japanese Geodetic Datum 2000 (JGD2000) and the M7005 bathymetry uses the Tokyo Datum for vertical and World Geodetic System 1984 (WGS84) for horizontal, a combination nearly identical to JGD2000. Both JGD2000 and the Tokyo Datum use mean sea level in Tokyo Bay as 0-m elevation. Vertical errors associated with combining these data sets are likely small.

Publicly available ASTER GDEM topographic data with grid resolution of 30 m is not very accurate in coastal areas. Infrastructure that affects the dynamics of tsunami inundation, such as tsunami walls, also is poorly modeled in the GDEM. Therefore, for topography data below 50-m elevation, we manually digitized topographic contours from the GSI maps to include tsunami walls and improve the coastline, and used the ASTER GDEM data as the background topographic data. We combined all of these data sets using ArcGIS 9.1 software.

Earthquake Sources

Earthquake slip distributions for the inversions used in this study were obtained through the following means:

- 1 used the GCMT parameters for earthquake found at the Global Centroid Moment Tensor Project database, <http://www.globalcmt.org/CMTsearch.html> (last accessed March 2012).
- 2 (as in Hayes, 2011) is available at http://www.earthquake.usgs.gov/earthquakes/eqinthenews/2011/usc0001xgp/results/static_out (last accessed May 2011).
- 3 (as in Shao *et al.*, 2011) is available at http://www.geol.ucsb.edu/faculty/ji/big_earthquakes/2011/03/0311_v3/Honshu.html (last accessed May 2011).
- 4 (as in Ammon *et al.*, 2011) is available at <http://eqseis.geosc.psu.edu/~cammon/Japan2011EQ/> (last accessed March 2012).

B. T. MacInnes, A. R. Gusman, R. J. LeVeque, and Y. Tanioka

- 5 is available at http://www.tectonics.caltech.edu/slip_history/2011_taiheiyoko/ (last accessed May 2011).
- 6 can be found in Fujii *et al.* (2011).
- 7 (Saito *et al.*, 2011), 8a and 8b (Gusman *et al.*, 2012), and 9 (Tang *et al.*, 2012; Wei *et al.*, 2012) were obtained directly from the authors.

Other Data Sources Used in This Study

- DART records were downloaded from the NDBC website http://www.ndbc.noaa.gov/to_station.shtml (last accessed March 2012).
- Measurements of coastal subsidence were obtained from the *Preliminary GPS coseismic displacement data for March 11, 2011. M 9 Japanese earthquake* provided by the ARIA team at JPL and Caltech at <ftp://sideshow.jpl.nasa.gov/pub/usrs/ARIA/> (last accessed March 2012).
- Field survey results from Mori *et al.* (2012) can be found at <http://www.coastal.jp/tsunami2011/> (last accessed March 2012). Inundation maps were obtained from *Reference material No. 1 of the 5th special committee meeting for the investigation of earthquake and tsunami counter measures learning from the Tohoku-oki earthquake, Central Disaster Prevention Council in Japan* (in Japanese), <http://www.bousai.go.jp/jishin/chubou/higashinohon/5/sub1.pdf> (last accessed March 2012).
- Videos of tsunami inundation in Taro and of the arrival time of the tsunami at the Sendai airport are available online. Examples include
 1. Taro: <http://www.nbcnews.com/video/nbc-news/42075714#42075714> (last accessed March 2012).
 2. Taro: <http://www.youtube.com/watch?v=xBktw9JMba4> (last accessed March 2012).
 3. Sendai: <http://www.youtube.com/watch?v=6FvJ62qvLBY> (last accessed March 2012).

Acknowledgments

This research was made possible by NSF Grant Numbers DMS-1137960 and DMS-0914942, the JSPS Postdoctoral Fellowship for Foreign Researchers program, and the Founders Term Professorship in Applied Mathematics.

References

- Aida, I. (1978). Reliability of a tsunami source model derived from fault parameters, *J. Phys. Earth* **26**, 57–73.
- Amante, C., and B. W. Eakins (2009). ETOPO1 1 arc-minute global relief model: Procedures, data sources and analysis, NOAA Technical Memorandum NESDIS NGDC-24, National Geophysical Data Center, U.S. Department of Commerce, Boulder, Colorado, 19 pp.
- Ammon, C. J., T. Lay, H. Kanamori, and M. Cleveland (2011). A rupture model of the great 2011 Tohoku earthquake, *Earth Planets Space* **63**, 693–696.
- Arcas, D., and V. V. Titov (2009). Sumatra tsunami: Lessons from modeling, *Surv. Geophys.* **27**, 679–705, doi: 10.1007/s10712-006-9012-5.
- Berger, M. J., D. L. George, R. J. LeVeque, and K. T. Mandli (2011). The GeoClaw software for depth-averaged flows with adaptive refinement, *Adv. Water Resour.* **34**, 1195–1206.

- Fujii, Y., K. Satake, S. Sakai, M. Shinohara, and T. Kanazawa (2011). Tsunami source of the 2011 off the Pacific coast of Tohoku Earthquake, *Earth Planets Space* **63**, 815–820.
- George, D. L. (2008). Augmented Riemann solvers for the shallow water equations over variable topography with steady states and inundation, *J. Comp. Phys.* **227**, 3089–3113.
- George, D. L., and R. J. LeVeque (2006). Finite volume methods and adaptive refinement for global tsunami propagation and local inundation, *Science of Tsunami Hazards* **24**, 319–328.
- Gonzalez, F., R. J. LeVeque, P. Chamberlain, B. Hirai, J. Varkovitzky, and D. L. George (2011). GeoClaw Results for the NTHMP Tsunami Benchmark Problems, (NTHMP) National Tsunami Hazard Mitigation Program (2012), in *Proceedings and Results of the 2011 NTHMP Model Benchmarking Workshop*, Boulder, U.S. Department of Commerce/NOAA/NTHMP (NOAA Special Report), 436 pp.
- Grilli, S. T., J. C. Harris, T. Tajalibakhsh, T. L. Masterlark, C. Kyriakopoulos, J. T. Kirby, and F. Shi (2012). Numerical simulation of the 2011 Tohoku tsunami based on a new transient FEM co-seismic source: Comparison to far- and near-field observations, *Pure Appl. Geophys.* doi: 10.1007/s00024-012-0528-y.
- Gusiakov, V. K. (1978). Static displacement on the surface of an elastic space, ill-posed problems of mathematical physics and interpretation of geophysical data, *Comput. Cent. of Sov. Acad. of Sci. Novosibirsk, Russia*, 23–51 (in Russian).
- Gusman, A. R., Y. Tanioka, S. Sakai, and H. Tsushima (2012). Source model of the great 2011 Tohoku earthquake estimated from tsunami waveforms and crustal deformation data, *Earth Planet. Sci. Lett.* **341–344**, 234–242, doi: 10.1016/j.epsl.2012.06.006.
- Hayes, G. P. (2011). Rapid source characterization of the 03-11-2011 M_w 9.0 off the Pacific coast of Tohoku earthquake, *Earth Planets Space* **63**, 1–6.
- Ide, S., A. Baltay, and G. C. Beroza (2011). Shallow dynamic overshoot and energetic deep rupture in the 2011 M_w 9.0 Tohoku-Oki earthquake, *Science* **332**, no. 6036, 1422–1429, doi: 10.1126/science.1207020.
- Iinuma, T., M. Ohzono, Y. Ohta, and S. Miura (2011). Coseismic slip distribution of the 2011 off the Pacific coast of Tohoku earthquake (M 9.0) estimated based on GPS data: Was the asperity in Miyagi-oki ruptured? *Earth Planets Space* **63**, 643–648.
- Johnson, J. M. (1998). Heterogeneous coupling along the Alaska-Aleutians as inferred from tsunami, seismic, and geodetic inversions, *Adv. Geophys.* **39**, 1–116.
- Kajiya, K. (1963). The leading wave of a tsunami, *Bull. Earthq. Res. Inst. Tokyo Univ.* **41**, 545–571.
- Kawamura, K., T. Sasaki, T. Kanamatsu, and A. Sakaguchi (2012). Large submarine landslides in the Japan trench: A new scenario for additional tsunami generation, *Geophys. Res. Lett.* **39**, L05308, 5 pp., doi: 10.1029/2011GL050661.
- Koketsu, K., Y. Yokota, N. Nishimura, Y. Yagi, S. Miyazaki, K. Satake, Y. Fujii, H. Miyake, S. Sakai, Y. Yamanaka, and T. Okada (2011). A unified source model for the 2011 Tohoku earthquake, *Earth Planet. Sci. Lett.* **310**, 480–487.
- Koper, K. D., A. R. Hutko, T. Lay, C. J. Ammon, and H. Kanamori (2011). Frequency-dependent rupture process of the 11 March 2011 M_w 9.0 Tohoku earthquake: Comparison of short-period P wave backprojection images and broadband seismic rupture models, *Earth Planets Space* **63**, 599–602.
- Lay, T., Y. Yamazaki, C. J. Ammon, K. F. Cheung, and H. Kanamori (2011). The 2011 M_w 9.0 off the Pacific coast of Tohoku Earthquake: Comparison of deep-water tsunami signals with finite-fault rupture model predictions, *Earth Planets Space* **63**, no. 7, 797–801, doi: 10.5047/eps.2011.05.030.
- LeVeque, R. J. (2002). *Finite Volume Methods for Hyperbolic Problems*, Cambridge University Press, 64–84, 100–123.
- Maeda, T., T. Furumura, S. Sakai, and M. Shinohara (2011). Significant tsunami observed at ocean-bottom pressure gauges during the 2011 off the Pacific coast of Tohoku earthquake, *Earth Planets Space* **63**, 803–808.
- Mori, N., and T. Takahashi (2012). The 2011 Tohoku earthquake tsunami joint survey group (2012). Nationwide post event survey and analysis of the 2011 Tohoku earthquake tsunami, *Coast. Eng. J.* **54**, no. 1, 27 pp., doi: 10.1142/S0578563412500015.
- Okada, R. (1985). Surface deformation due to shear and tensile faults in a half-space, *Bull. Geol. Soc. Am.* **75**, no. 4, 1135–1154.
- Pietrzak, J., A. Socquet, D. Ham, W. Simons, C. Vigny, R. J. Labeur, E. Schrama, G. Stelling, and D. Vatvani (2007). Defining the source region of the Indian Ocean tsunami from GPS, altimeters, tide gauges and tsunami models, *Earth Planet. Sci. Lett.* **261**, 49–64.
- Poisson, B., C. Oliveros, and R. Pedreros (2011). Is there a best source model of the Sumatra 2004 earthquake for simulating the consecutive tsunami? *Geophys. J. Int.* **185**, 1365–1378, doi: 10.1111/j.1365-246X.2011.05009.x.
- Pollitz, F. F., R. Bürgmann, and P. Banerjee (2011). Geodetic slip model of the 2011 M 9.0 Tohoku earthquake, *Geophys. Res. Lett.* **38**, L00G08, 6 pp., doi: 10.1029/2011GL048632.
- Saito, T., Y. Ito, D. Inazu, and R. Hino (2011). Tsunami source of the 2011 Tohoku-Oki earthquake, Japan: Inversion analysis based on dispersive tsunami simulations, *Geophys. Res. Lett.* **38**, L00G19, 5 pp., doi: 10.1029/2011GL049089.
- Saito, T., K. Satake, and T. Furumura (2010). Tsunami waveform inversion including dispersive waves: The 2004 earthquake off Kii peninsula, Japan, *J. Geophys. Res.* **115**, no. B06303, 12 pp., doi: 10.1029/2009JB006884.
- Satake, K. (1995). Linear and nonlinear computations of the 1992 Nicaragua earthquake tsunami, *Pure Appl. Geophys.* **144**, 455–470.
- Shao, G., X. Li, C. Ji, and T. Maeda (2011). Focal mechanism and slip history of 2011 M_w 9.1 off the Pacific coast of Tohoku earthquake, constrained with teleseismic body and surface waves, *Earth Planets Space* **63**, 559–564.
- Shimozono, T., S. Sato, K. A. Okayasu, Y. Tajima, H. M. Fritz, H. Liu, and T. Takagawa (2012). Propagation and inundation characteristics of the 2011 Tohoku tsunami on the central Sanriku coast, *Coast. Eng. J.* **54**, no. 1250004, 17 pp., doi: 10.1142/S0578563412500040.
- Simons, M., S. E. Minson, A. Sladen, F. Ortega, J. Jiang, S. E. Owen, L. Meng, J. P. Ampuero, S. Wei, R. Chu, D. V. Helmlinger, H. Kanamori, E. Hetland, A. W. Moore, and F. H. Webb (2011). The 2011 magnitude 9.0 Tohoku-Oki earthquake: Mosaicking the megathrust from seconds to centuries, *Science* **332**, no. 6036, 1421–1425, doi: 10.1126/science.1206731.
- Tang, L., E. N. Bernard, V. V. Titov, Y. Wei, C. D. Chamberlin, M. Eble, C. Moore, J. C. Newman, M. Spillane, H. O. Mofjeld, and L. Wright (2012). Direct energy estimates of the 2011 Japan tsunami using deep-ocean pressure data for real-time forecasting, *J. Geophys. Res.* **117**, no. C08008, 28 pp., doi: 10.1029/2011JC007635.
- Tanioka, Y., and K. Satake (1996). Tsunami generation by horizontal displacement of ocean bottom, *Geophys. Res. Lett.* **23**, 861–864.
- Tanioka, Y., and T. Seno (2001). Sediment effect on tsunami generation of the 1896 Sanriku tsunami earthquake, *Geophys. Res. Lett.* **28**, no. 17, 3389–3392.
- Titov, V. V., and C. E. Synolakis (1998). Numerical modeling of tidal wave runup, *Journal of Waterway, Port, Coastal and Ocean Engineering* **124**, 157–171.
- Tsuji, T., Y. Ito, M. Kido, Y. Osada, H. Fujimoto, J. Ashi, M. Kinoshita, and T. Matsuoka (2011). Potential tsunamigenic faults of the 2011 Tohoku earthquake, *Earth Planets Space* **63**, 831–834.
- Wei, S., A. Sladen, and The ARIA group (2011). Updated Result 3/11/2011 (M_w 9.0), Tohoku-oki, Japan, http://www.tectonics.caltech.edu/slip_history/2011_taiheiyo-oki/, last accessed 30 March 2012.
- Wei, Y., C. Chamberlin, V. V. Titov, L. Tang, and E. N. Bernard (2012). Modeling of 2011 Japan tsunami—Lessons for near-field forecast, *Pure Appl. Geophys.* 1–23, doi: 10.1007/s00024-012-0519-z.
- Wei, Y., V. V. Titov, A. Newman, G. Hayes, L. Tang, and C. Chamberlin (2011). Near-field hazard assessment of March 11, 2011 Japan tsunami

- sources inferred from different methods, in *Proceedings of OCEANS 2011*, September 19–22 2011, Waikoloa, Hawaii, 1–9.
- Wei, Y., V. V. Titov, L. Tang, and C. Chamberlin (2011). Assessing the near-field tsunami hazard for the Pacific Northwest in view of the 2011 Japan tsunami (abstract NH13G-06), *AGU 1*, no. 6 (Fall Meet.), NH13G-06.
- Yamazaki, Y., T. Lay, K. F. Cheung, H. Yue, and H. Kanamori (2011). Modeling near-field tsunami observations to improve finite-fault slip models for the 11 March 2011 Tohoku earthquake, *Geophys. Res. Lett.* **38**, L00G15, 6 pp., doi: 10.1029/2011GL049130.
- Yim, S. C., K. F. Cheung, M. J. Olsen, and Y. Yamazaki (2012). Tohoku tsunami survey, modeling and probabilistic load estimation applications, in *Proc. of the International Symposium on Engineering Lessons Learned from the 2011 Great East Japan Earthquake*, 1–4 March 2012, Tokyo, Japan, 430–443.

B. T. MacInnes, A. R. Gusman, R. J. LeVeque, and Y. Tanioka

Institute of Seismology and Volcanology
Hokkaido University
N10W8 Kita-ku
Sapporo, Hokkaido 060-0810, Japan
macinnes@geology.cwu.edu
(B.T.M., A.R.G., Y.T.)

Department of Applied Mathematics
University of Washington
Box 352420
Seattle, Washington 98195-2420
(R.J.L.)

Manuscript received 31 March 2012